Radiative Damping Revisited: Parameterization of Damping Rate in the Middle Atmosphere

XUN ZHU

Department of Earth and Planetary Sciences, The Johns Hopkins University, Baltimore, Maryland

(Manuscript received 2 September 1992, in final form 24 February 1993)

ABSTRACT

Radiative damping rates of temperature perturbations are calculated by CO_2 and O_3 Curtis matrices extending from the surface to 120 km in the earth's atmosphere with the eigenvalue and scale-dependent Newtonian cooling methods at 0.5 km of vertical resolution. Based on the latest value of the deactivation rate of CO_2 bending mode by atomic oxygen, the radiative damping rate in the region of 90–100 km is $\sim 1.3\ \text{day}^{-1}$ due to the near-local thermodynamic equilibrium nature of CO_2 15-μm band emission. This is comparable to the damping rate induced by eddy and molecular diffusion of $\sim 2.5\ \text{day}^{-1}$ in the corresponding region. It is also found that the radiative damping of the temperature perturbation in the winter polar mesopause is more than a factor 3 greater than in the summer polar mesopause. A simple and accurate parameterization for the scale-dependent damping rate as a function of altitude for any temperature profile is derived and tested with a zonally averaged model atmosphere. The typical percentage error of such a simple parameterization is about 10%–20%. This parameterization can be used in models of wave–zonal flow interaction in the earth's middle atmosphere.

1. Introduction

Many authors have made efforts to determine the radiative damping rate of temperature perturbations in the earth's middle atmosphere (e.g., Dickinson 1973; Shved 1978; Shved and Utyakovskiy 1983; Fels 1982, 1984; Apruzese and Strobel 1984; Zhu and Strobel 1991). Generally speaking, the radiative heat exchange can be split into two components: radiation to space and exchange within the atmosphere. For an optically thin atmosphere the first component makes most of the contribution to the damping rate (e.g., Dickinson 1973). In the case of an optically thick atmosphere (e.g., Fels 1984) Spiegel's (1957) formula based on the approximation of an infinite, homogeneous atmosphere gives damping rate for an infinite harmonic temperature wave. It should be mentioned that whether a temperature perturbation is embedded in an optically thin or thick atmosphere is determined by the scale of the perturbation relative to the background field. Furthermore, it is always assumed that the background temperature profile remains fixed even in an optically thin atmosphere.

Theoretically, there are two approaches in studies: eigenvalue approach and Newtonian damping rate (Goody and Yung 1989). Practically, scale-dependent Newtonian damping rate, which describes decaying of a local wave packet with a characteristic vertical wavenumber, has the advantages of both approaches (Zhu and Strobel 1991). Calculation of the damping rate requires a complete solution of the radiative transfer equation. Because this is a time consuming procedure most authors present and test only scale-dependent damping rates for certain specific temperature profiles and/or in certain regions of the middle atmosphere. Recently, Zhu et al. (1992) proposed an algorithm to calculate the atmospheric cooling rate by a Curtis matrix interpolation of correlated-k coefficients. Based on this algorithm Curtis matrices can be accurately derived for any temperature profile in the whole atmosphere. The damping due to water vapor cooling in the middle atmosphere is neglected. The radiative heat exchange by CO_2 15-μm band and O_3 9.6-μm band provides most of the atmospheric cooling effect and the damping of a temperature perturbation. In this paper, we will propose and test a general formula to calculate the scale-dependent damping rate due to these two bands in the earth's middle atmosphere.

2. Radiative damping rates derived from eigenvalue approach

The cooling rate by CO_2 and O_3 in the atmosphere can be expressed in the form of Curtis matrices as follows (Zhu et al. 1992):

$$\mathbf{Q} \equiv d\mathbf{T}/dt = \mathbf{C}_2\theta_2 + \mathbf{C}_3\theta_3 \qquad (1)$$

where $\mathbf{C}_2$ and $\mathbf{C}_3$ are the Curtis matrices for CO_2 15-μm band and O_3 9.6-μm band, respectively; θ_2 and θ_3 are the vectors of Planck blackbody functions nor-

Corresponding author address: Dr. Xun Zhu, The Johns Hopkins University, Department of Earth and Planetary Sciences, Baltimore, MD 21218.

malized at a reference temperature $T = 250$ K and band center frequencies ν_i

$$\theta_i(k) = \frac{B(\nu_i, T_k)}{B(\nu_i, 250)}, \quad k = 1, 2, \cdots, M. \quad (2)$$

Setting $\nu_2 = 675\ \text{cm}^{-1}$ and $\nu_3 = 1075\ \text{cm}^{-1}$ for CO_2 and O_3, we then get θ_i at level k

$$\theta_2(k) = \frac{47.6}{\exp(971.0/T_k) - 1},$$

$$\theta_3(k) = \frac{484}{\exp(1546/T_k) - 1}. \quad (3a,b)$$

If we neglect the variation of the Curtis matrices with respect to a small temperature perturbation $\delta\mathbf{T}$, then the relaxation of $\delta\mathbf{T}$ is derived from (1) as (Zhu and Strobel 1991)

$$\frac{d(\delta\mathbf{T})}{dt} = \mathbf{C}_2\left[\frac{\partial\theta_2}{\partial\mathbf{T}}\right]\delta\mathbf{T} + \mathbf{C}_3\left[\frac{\partial\theta_3}{\partial\mathbf{T}}\right]\delta\mathbf{T} \equiv \mathbf{A}\delta\mathbf{T}. \quad (4)$$

The $M \times M$ matrix $\mathbf{A}$ defined in (4) is determined by the basic temperature field $\mathbf{T}$

$$\mathbf{A} = \mathbf{C}_2\left[\frac{\partial\theta_2}{\partial\mathbf{T}}\right] + \mathbf{C}_3\left[\frac{\partial\theta_3}{\partial\mathbf{T}}\right] \equiv \mathbf{A}_2 + \mathbf{A}_3. \quad (5)$$

Furthermore, $[\partial\theta_2/\partial\mathbf{T}]$ and $[\partial\theta_3/\partial\mathbf{T}]$ are diagonal matrices of elements

$$\frac{\partial\theta_2(k)}{\partial T_k} = \frac{4.62 \times 10^4}{T_k^2[\exp(971.0/T_k) - 1]^2}\exp\left(\frac{971.0}{T_k}\right) \approx \frac{4.62 \times 10^4}{T_k^2}\exp\left(-\frac{971.0}{T_k}\right), \quad (6a)$$

$$\frac{\partial\theta_3(k)}{\partial T_k} = \frac{7.48 \times 10^5}{T_k^2[\exp(1546/T_k) - 1]^2}\exp\left(\frac{1546}{T_k}\right) \approx \frac{7.48 \times 10^5}{T_k^2}\exp\left(-\frac{1546}{T_k}\right). \quad (6b)$$

Our numerical calculations to certain examples show that the errors produced by neglecting the Curtis matrix variations due to a temperature perturbation $\delta\mathbf{T}$ are small ($\leqslant 20\%$). In appendix A we will further assess the errors analytically under conditions of weak or strong absorption and a cool-to-space approximation. Equation (4) is a linear system describing the radiative damping of a temperature perturbation from a basic temperature field. As shown in Zhu and Strobel (1991), the solution of (4) is determined by all the eigenvectors and the eigenvalues of $\mathbf{A}$. In this section we will perform the same analysis as in Zhu and Strobel (1991) but with the matrix $\mathbf{A}$ extending from -0.5 km to 120 km with a vertical resolution of 0.5 km and including both CO_2 15-μm and O_3 9.6-μm bands. At the lower boundary the upward flux is set to be the blackbody radiance, while at the upper boundary the downward flux is set at zero. Although the model includes both troposphere and middle atmosphere, our results can be applied only to the middle atmosphere because in the troposphere additional cooling by H_2O and clouds becomes dominant. The 242×242 Curtis matrix for CO_2 15-μm band ($500\ \text{cm}^{-1}$–$850\ \text{cm}^{-1}$) $\mathbf{C}_2$ is calculated as in Zhu et al. (1992) for the *U.S. Standard Atmosphere (1976)* but with the k distribution derived from a line-by-line integration and with $\Delta\nu_n = 25\ \text{cm}^{-1}$ and $I = 30$ (g_i points). For O_3 9.6-μm band ($980\ \text{cm}^{-1}$–$1180\ \text{cm}^{-1}$) the Curtis matrix $\mathbf{C}_3$ is calculated the same as $\mathbf{C}_2$ but with $\Delta\nu_n = 40\ \text{cm}^{-1}$ and $I = 20$. The reason that we need more g_i points for CO_2 15-μm band than O_3 9.6-μm band is that the half-widths of the k coefficient (Zhu 1992) for CO_2 15-μm band are much smaller.

It is known that above 80 km the atmospheric cooling rate by CO_2 15-μm band is significantly affected by various non-local thermodynamic equilibrium (non-LTE) processes (e.g., Kutepov and Shved 1978; Dickinson 1984). Recent studies of upper-atmospheric CO_2 15-μm band emission (Sharma and Wintersteiner 1990) and laboratory measurements (Shved et al. 1991) show that the deactivation rate of CO_2 bending mode by atomic oxygen, $K_{CO_2\text{-}O}$, is one order of magnitude greater than those used in previous non-LTE models. A larger value of $K_{CO_2\text{-}O}$ significantly increases the cooling rate by CO_2 15-μm band in the lower thermosphere (Shved et al. 1991) because it restores the CO_2 $\nu_2 = 1$ population closer to LTE (Lopez-Puertas et al. 1992). The radiative damping rate is directly related to the cooling rate through the Curtis matrices. Therefore, larger values of $K_{CO_2\text{-}O}$ also enhance the radiative damping of waves in the lower thermosphere. We will show below that damping of a temperature perturbation by radiation is comparable to its dissipation induced by eddy and molecular diffusion between 90 and 100 km.

In Fig. 1 the total cooling rate $\mathbf{Q}$ (solid line) for the background atmosphere based on the Curtis matrices $\mathbf{C}_2$ and $\mathbf{C}_3$ is presented from the surface up to 120 km. The deactivation rate used in the calculation $K_{CO_2\text{-}O} = 5.5 \times 10^{-12}\ \text{cm}^3\ \text{s}^{-1}$ is taken from a recent study by Wintersteiner et al. (1992). The CO_2 mixing ratio is also adopted from Wintersteiner et al. (1992) by taking an average of two model profiles representing higher and lower ranges. The mixing ratio of atomic oxygen is adopted from the CIRA 1986 reference atmosphere. We see from the figure that the cooling rate increases rapidly with the altitude in the lower thermosphere due to the rapidly increased temperature. It reaches maximum value of $\sim 50\ \text{K day}^{-1}$ around 117 km. Above that level the non-LTE effect dominates over temperature increase so the cooling rate decreases rapidly with the altitude. These results are consistent with the more detailed calculations by Wintersteiner et al. (1992). The thin line in the figure gives the total cooling rate under the LTE conditions. We see that significant differences occur only above ~ 100 km. Also shown

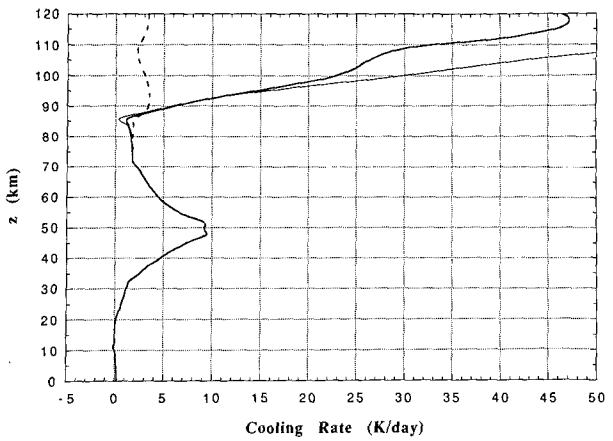

FIG. 1. The total non-LTE (solid line) and LTE (dash line) cooling rates by CO_2 15-μm band and O_3 9.6-μm band for the *U.S. Standard Atmosphere, 1976*. The open circles denote the non-LTE cooling rate based on the previously used deactivation rate of CO_2 bending mode by atomic oxygen.

in the figure (dashed line) is the cooling rate calculated with the deactivation rate used in previous studies (Lopez-Puertas et al. 1986) $K^*_{CO_2\text{-}O} = 1.0 \times 10^{-14}\sqrt{T} + 2.32 \times 10^{-9}\exp(-76.75/T^{1/3})$ cm^3 s^{-1}. Under atmospheric conditions around the mesopause, this gives $K^*_{CO_2\text{-}O} = 1.4 \times 10^{-13}$ cm^3 s^{-1}. Figure 1 shows that with the new value of $K_{CO_2\text{-}O}$ the cooling rate around 100 km has been increased by a factor of 7 because it only slightly departs from the LTE cooling rate.

In Fig. 2 we show six eigenvectors together with the corresponding eigenvalues for the matrix **A**. The minimum and maximum damping rates are $\lambda = 0.0030$ day^{-1} and $\lambda = 1.9792$ day^{-1}, respectively. The eigenvector corresponding to the minimum eigenvalue is a large-scale temperature disturbance peaked at 11 km (Fig. 2a) where the atmospheric cooling rate reaches its minimum value as shown in Fig. 1. On the other hand, the eigenvector corresponding to the maximum eigenvalue is a local wave packet centered at 73.5 km (Fig. 2d) with a vertical wavenumber of $2\pi/(1$ km). We note that Fig. 1 does not show any significance in cooling rate around 73.5 km for the background atmosphere. It is the radiative heat exchange among those nearby temperature maxima and minima that efficiently damps the wave packet. This example illustrates the scale-dependent nature of the damping rate. To further illustrate this point, two additional eigenvectors are shown in Figs. 2b and 2c. The scale-dependent nature has been largely explored in Zhu and Strobel (1991). When the vertical wavenumber of a temperature perturbation increases, the radiative heat exchange among the temperature maxima and minima also increases, and so does the damping rate of the temperature perturbation. The other notable character in Figs. 2a–d is that the eigenmodes appear localized in space. This is mainly caused by the vertical inhomogeneity of temperature and absorption coefficient in the background atmosphere. Above 90 km the atmosphere is optically thin and the escape probability for a photon in CO_2 15-μm band is greater than 0.3 (Zhu et al. 1992). A temperature disturbance is also damped in great part by different rates of cool to space at maxima and minima. In such a transparent limit, the scale dependence of the damping rate becomes less important. As shown in Zhu and Strobel (1991), the eigenvector for the transparent limit is a locally peaked delta function and the damping rate is independent on the vertical scale of the temperature perturbation. Figure 2e represents such an example of a temperature perturbation locally peaked at 111.5 km. In general, eigenmodes resemble neither sinusoidal waves nor locally peaked delta functions because of the inhomogeneity and opacity. One example is shown in Fig. 2f. We may consider that the eigenmode is made of two components. One is a wave disturbance in the mesosphere with a vertical wavelength of ~9 km. The other is a locally peaked perturbation located at 115 km. They both decay in the same damping rate of ~0.54 day^{-1}.

Although the cooling rate (Fig. 1) at 111.5 km (38.3 K day^{-1}) is ~20 times greater than that at 73.5 km (1.76 K day^{-1}) the damping rate at 111.5 is only ~1/3 of that at 73.5 km for a temperature perturbation with a vertical wavenumber of $2\pi/(1$ km). The reason is that the radiative heat exchange among the nearby maxima and minima does not enhance the damping in the transparent limit. This example also provides us a justification for neglecting the damping rate by H_2O in the middle atmosphere. Cooling by H_2O in the stratosphere could be as important as O_3 and CO_2. However, the concentration of H_2O in the stratosphere is so low that those nearby-layer heat exchanges are small. On the other hand, nearby-layer heat exchanges by CO_2 and O_3 make major contributions to the scale-dependent radiative damping rates. We will come back to this point in the next section.

To quantitatively show a general scale-dependent nature of the damping rate and its departure from a precise one we perform Fourier transforms and calculate the power spectral densities (PSDs) of all 242 eigenvectors (Zhu and Strobel 1991). The quantitative relation between the damping rate (λ) and maximum PSD wavenumber (n) is plotted in Fig. 3. Also shown in Fig. 3 are two analytical fits:

$$\lambda(n) = 0.40 + 2.22\left[1 - \frac{\tan^{-1}(0.74n)}{0.74n}\right], \quad (7)$$

$$\lambda(n) = 0.40 + \frac{1.85n^2}{6.93 + n^2}. \quad (8)$$

The form of the analytic expression (7) is derived by Spiegel's infinite, homogeneous model plus a radiation-

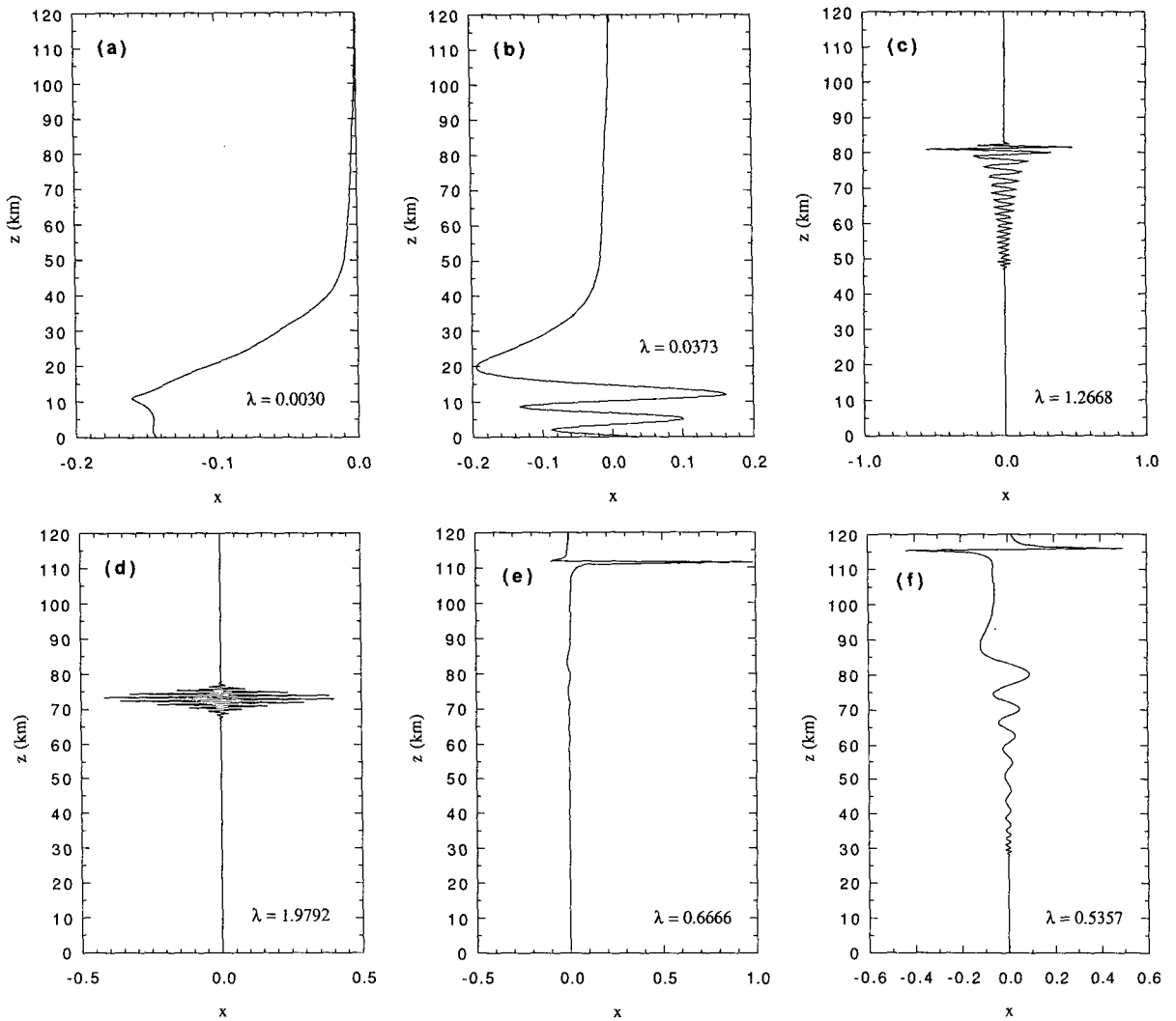

FIG. 2. Six eigenvectors together with their eigenvalues calculated according to a 242 × 242 matrix **A** defined in (5). The vertical resolution of all modes is 0.5 km. The first four eigenvectors (a)–(f) are typical. Their eigenvalues increase with the characteristic wavenumber. The panel (e) is a locally peaked delta function and the panel (f) is a general case for an inhomogeneous atmosphere. See the text for detailed discussions.

to-space term of 0.40 day^{-1} (Spiegel 1957; Goody and Yung 1989; Zhu and Strobel 1991). Expression (8) is derived with additional diffusivity approximation (Zhu and Strobel 1991). We see from Fig. 3 that either the scale-dependent damping rate expression describes damping rates of many eigenmodes. Because of the inhomogeneity of the atmosphere, however, some eigenmodes deviate significantly from these expressions. Had the real atmosphere been homogeneous, all the eigenmodes would be lined along a monotonic function. We could consider the diversion of the eigenmodes on a λ–n diagram as a measurement of the radiative inhomogeneity of the atmosphere.

Because of the nonuniqueness of the damping rate λ and vertical wavenumber n as shown in Fig. 3, the eigenvalue approach is not a practical tool describing a damping process of a wave packet in an inhomogeneous atmosphere. It is the vertical structure and location of a temperature disturbance that determine its damping rate in a vertically inhomogeneous atmosphere. The scale-dependent Newtonian damping rate given in the next section provides the best description of wave packet damping in the atmosphere even though the Newtonian damping rate is not an eigenvalue of **A** in general.

It should also be pointed out that only in an eigenvalue approach can the total damping be calculated by Fourier analyzing any arbitrary temperature perturbation and calculating the damping rate of each component. To illustrate this point let us consider the exact solution of (4). The solution can be formally written as

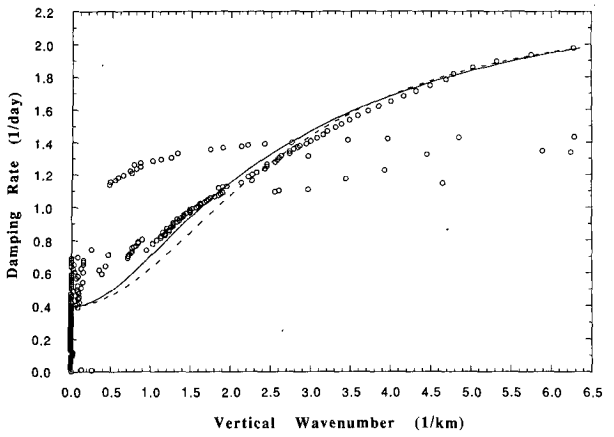

FIG. 3. A quantitative relation between the damping rate and the wavenumber at which the power spectral density is maximally peaked. Also shown in the figure are two analytic fits given by (7) (solid line) and (8) (dash line), respectively.

$$\delta\mathbf{T} = \exp(\mathbf{A}t)\delta\mathbf{T}_0, \tag{9}$$

where $\delta\mathbf{T}_0$ is the initial temperature perturbation. Following Zhu and Strobel (1991), we denote $-\lambda_j$ and $\mathbf{x}_j$ as eigenvalues and eigenvectors of $\mathbf{A}$

$$\mathbf{A}\mathbf{x}_j = -\lambda_j\mathbf{x}_j. \tag{10}$$

The fundamental solution $\exp(\mathbf{A}t)$ can be calculated from the eigenmodes of $\mathbf{A}$ (Lancaster 1969) and (9) can be rewritten as

$$\delta\mathbf{T} = \sum_{j=1}^{M} \beta_j\mathbf{x}_j \exp(-\lambda_j t), \tag{11}$$

where β_j is determined by the initial temperature perturbation

$$\sum_{j=1}^{M} \beta_j\mathbf{x}_j = \delta\mathbf{T}_0. \tag{12}$$

We have also assumed in (11) that all the eigenvalues are distinct. This assumption is strictly held at present. Expression (11) gives a precise description of the radiative damping for an initial temperature perturbation with an arbitrary structure $\delta\mathbf{T}_0$. Since the sinusoidal modes corresponding to scale-dependent Newtonian damping rates $\lambda(z, n)$ defined in the next section generally do not form a set of eigenmodes of $\mathbf{A}$, we cannot use (11) and (12) to describe the total damping by those Newtonian damping rates.

3. Scale-dependent Newtonian damping rate and its parameterization

We note that (4) can be considered as a discretized form of the integral equation

$$\frac{d[\delta T(z)]}{dt} = \int_{-\infty}^{\infty} K(z, \zeta)\delta T(\zeta)d\zeta. \tag{13}$$

It was shown in Zhu and Strobel (1991) that the following form for the Newtonian damping rate,

$$\lambda(z, n) = -\int_{-\infty}^{\infty} K(\zeta, z)\cos[n(\zeta - z)]d\zeta, \tag{14}$$

makes eigenvalue approach and traditional Newtonian cooling method equivalent in two important limits when the kernel function $K(\zeta, z)$ is given by (Zhu and Strobel 1991),

transparent limit:

$$K(\zeta, z) = -[\lambda(\zeta)\lambda(z)]^{1/2}\delta_{jk}(\zeta - z); \tag{15a}$$

homogeneous limit: $$K(\zeta, z) = K(|\zeta - z|); \tag{15b}$$

where δ_{jk} is the Dirac δ function. The eigenfunctions corresponding to the limits (15a) and (15b) are δ functions and sinusoidal harmonic waves, respectively (Zhu and Strobel 1991). In general, $\lambda(z, n)$ is a damping rate of a wave packet located at the altitude z with a characteristic vertical wavenumber n.

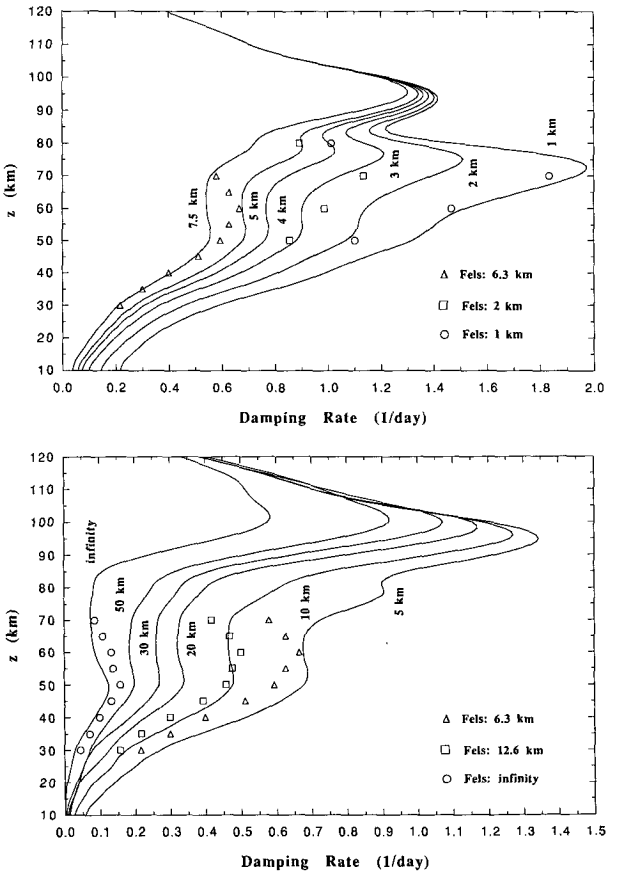

FIG. 4. Scale-dependent Newtonian damping rates of temperature perturbations in the middle atmosphere calculated by CO_2 and O_3 Curtis matrices. Panels (a) and (b) represent shorter and longer vertical wavelengths, respectively. Previous calculations by Fels (1982, 1984) are also shown in the figure.

In Fig. 4 we present the scale-dependent Newtonian damping rates in the middle atmosphere calculated by (14). For adjacent layers of $|\zeta - z| \leq 1$ km the integration in (14) is evaluated in a higher resolution by an analytic expression for $K(\zeta, z)$ that matches the actual values at grid points. From Fig. 4 we note that the damping rate for a wave packet of 1-km vertical wavelength around 73 km is 1.98 day^{-1}. This value, which corresponds to an optically thick condition, is identical to the results in Fig. 2d derived from the eigenvalue approach. Furthermore, a damping rate of $\sim$0.67 day^{-1} at 111.5 km shown in Fig. 4 is consistent with the eigenvalue given in Fig. 2e for an optically thin absorption. Also shown in Fig. 4 are the damping rates by Fels (1982, 1984). The largest differences occur above 70 km (Fig. 4a) where the present damping rate is significantly larger than that by Fels (1984). This is primarily due to the difference in the treatment of non-LTE processes. In Fels (1984), breakdown of LTE starts around 70 km. At 80 km the non-LTE damping rate is about half of the LTE damping rate.

In Fig. 5 we show two magnifications of Fig. 4 in

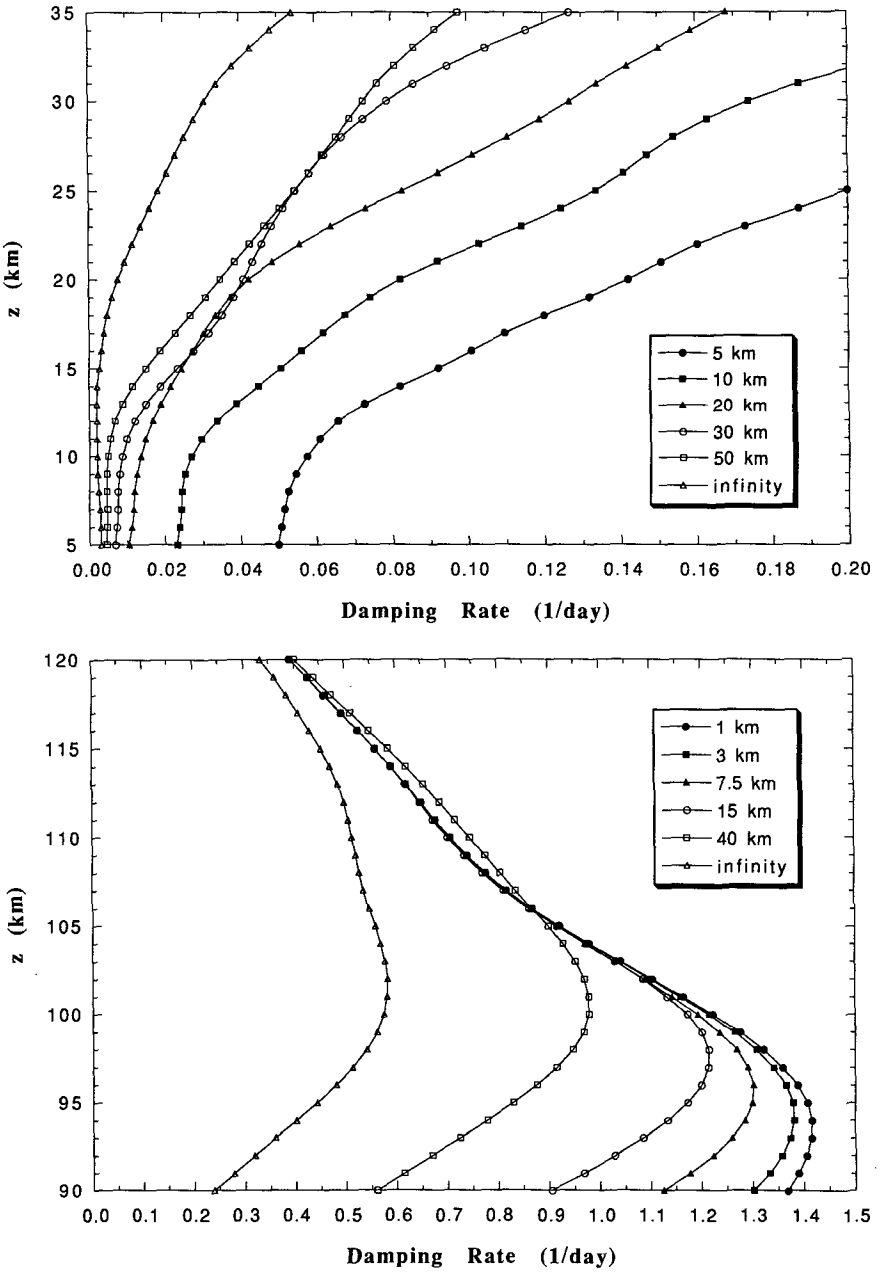

FIG. 5. Magnification of Fig. 4 in the region of (a) 5–35 km and (b) 90–120 km, respectively.

two domains. One is the damping rate for wavelengths longer than 10 km in the region below 35 km (Fig. 5a) where the damping rate is small. The other is the region from 90 km to 120 km (Fig. 5b) where with the increase of the altitude the transparent limit becomes a better approximation and the dependence of the damping rate on the vertical scale becomes weaker. At 100 km the difference of the damping rates for vertical wavelengths of 1 km and 40 km is less than 20%. Above 100 km the cooling rate is quite sensitive to the atmospheric parameters of temperature and CO_2 and O concentrations (Lopez-Puertas et al. 1992). Furthermore, the damping rate in the transparent limit is directly proportional to the cooling rate. Hence, the damping rate above 100 km also shows sensitive variations when those parameters change. However, a simple analytical expression is available for the damping rate at the transparent limit (Goody and Yung 1989).

Figure 4 also shows a local maximum in damping rate around 95 km. To compare the radiative damping rate with the damping induced by eddy and molecular diffusion in the region of 90–100 km, we first note that the damping rate of a gravity wave induced by eddy and molecular diffusion can be approximated by (Zhu 1987)

$$\Lambda = K_{zz}\left(n^2 - \frac{1}{4H^2}\right)(1 + \mathrm{Pr}^{-1}), \qquad (16)$$

where K_{zz} is the diffusion coefficient, H is the scale height, and Pr is the Prandtl number. In the region of 90–100 km we set (Holton 1983; Strobel 1989) $K_{zz} = 20\ \mathrm{m^2\ s^{-1}}$, Pr = 3, $n = 2\pi/H$, and $H = 6$ km. Substituting these values into (16) we get $\Lambda = 2.5\ \mathrm{day^{-1}}$. From Fig. 5b we see that the corresponding radiative damping rate in the region is $\lambda \approx 1.3\ \mathrm{day^{-1}}$, which is comparable to the damping rate induced by eddy and molecular diffusion. Below 90 km, gravity wave breaking produces larger eddy diffusion coefficient (Lindzen 1981; Strobel 1989), and above 100 km molecular diffusion increases rapidly with the altitude. It should be pointed out that if the previous value of $K^*_{CO_2\text{-}O} = 1.4 \times 10^{-13}\ \mathrm{cm^3\ s^{-1}}$ were used, the radiative damping rate in the region of 90–100 km is only $\lambda \approx 0.33\ \mathrm{day^{-1}}$ and eddy and molecular diffusion would control the dissipation of waves.

The damping rates in Figs. 4 and 5 are based on a standard temperature profile. To apply these results to a realistic model of wave–zonal flow interaction a simple expression of damping rate for any temperature profile is desirable. Guided by the results in Fig. 3 we specify the kernel function in (14) as

$$K(\zeta, z) = -N_0 - N_\infty[\delta_{jk}(r) - (k_m/2)E_1(k_m r)], \qquad (17)$$

where $E_1(k_m r)$ is the exponential integral, k_m is the mean absorption coefficient, and $r = |z - \zeta|$. Substituting (17) into (14) results in the following analytic expression for the damping rate for a reference temperature profile

$$\lambda_r(z, n) = N_0 + N_\infty\left[1 - \frac{\tan^{-1}(n/k_m)}{(n/k_m)}\right]. \qquad (18)$$

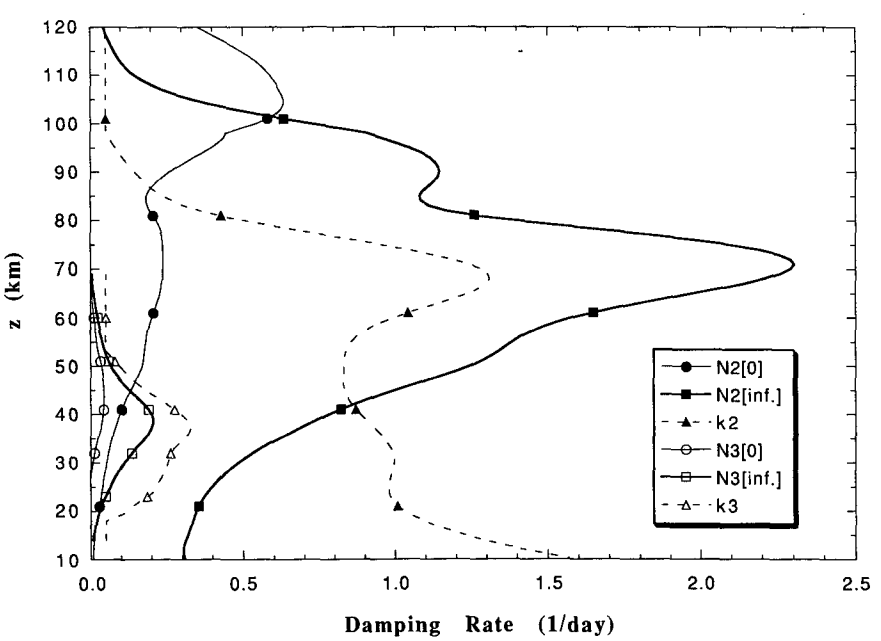

FIG. 6. Damping rate parameters used in (14) for a referenced atmosphere. N2[0], N2[inf], and k2 are used to calculate the damping rate by CO_2 15-μm band. N3[0], N3[inf], and k3 are used to calculate the damping rate by O_3 9.6-μm band.

At this stage we can let N_0, N_∞, and k_m all vary with the altitude. For a given altitude z (or pressure p with $p_s = 1013.25$ mb) these parameters can be determined by a nonlinear least-squares fit for a set of λ_r and n (Press et al. 1986). The parameters for CO_2 and O_3 are given in Fig. 6. These parameters together with a reference temperature profile are presented numerically in Table 1. In real applications Table 1 could be stored at model grid points as a lookup file. It should be noted that because parameters shown in Fig. 6 are derived by fitting (18) to the data in Fig. 4, they will be most accurate for damping rates with disturbances of characteristic vertical wavelengths greater than 1 km.

The first term on the right-hand side of (18) is in-

TABLE 1. Damping rate parameters derived from least-squares fitting.

z (km)	T (K)	$\mathrm{Log}_{10}(p/p_s)$	$N_0^{CO_2}$	$N_\infty^{CO_2}$	$k_m^{CO_2}$	$N_0^{O_3}$	$N_\infty^{O_3}$	$k_m^{O_3}$
120	360.45	−7.666	0.355	0.045	0.050	0.000	0.000	0.050
118	336.45	−7.583	0.412	0.055	0.050	0.000	0.000	0.050
116	312.45	−7.495	0.468	0.070	0.050	0.000	0.000	0.050
114	288.45	−7.400	0.520	0.087	0.050	0.000	0.000	0.050
112	264.45	−7.296	0.559	0.110	0.050	0.000	0.000	0.050
110	240.45	−7.182	0.588	0.146	0.050	0.000	0.000	0.050
108	223.74	−7.058	0.610	0.200	0.050	0.000	0.000	0.050
106	213.35	−6.927	0.627	0.281	0.050	0.000	0.000	0.050
104	205.76	−6.790	0.633	0.396	0.050	0.000	0.000	0.050
102	199.98	−6.648	0.609	0.546	0.050	0.000	0.000	0.050
100	195.53	−6.502	0.542	0.725	0.050	0.000	0.000	0.050
98	192.18	−6.354	0.446	0.907	0.053	0.000	0.000	0.050
96	189.76	−6.203	0.420	1.004	0.073	−0.002	0.004	0.050
94	188.19	−6.050	0.368	1.086	0.094	−0.003	0.006	0.050
92	187.42	−5.897	0.311	1.133	0.117	−0.005	0.009	0.050
90	187.32	−5.743	0.260	1.147	0.145	−0.006	0.011	0.050
88	187.33	−5.589	0.218	1.129	0.177	−0.006	0.011	0.050
86	187.75	−5.435	0.191	1.094	0.216	−0.005	0.009	0.050
84	190.70	−5.282	0.184	1.086	0.271	−0.003	0.005	0.050
82	194.61	−5.132	0.196	1.168	0.364	0.000	0.000	0.050
80	198.55	−4.984	0.216	1.383	0.505	0.000	0.000	0.050
78	202.49	−4.840	0.231	1.685	0.680	0.000	0.000	0.050
76	206.43	−4.698	0.237	1.978	0.865	0.000	0.000	0.050
74	210.37	−4.559	0.238	2.190	1.041	0.000	0.000	0.050
72	214.48	−4.422	0.238	2.293	1.186	0.000	0.000	0.050
70	219.59	−4.289	0.238	2.292	1.279	0.000	0.000	0.050
68	225.07	−4.158	0.237	2.206	1.310	0.002	0.006	0.050
66	230.57	−4.030	0.233	2.060	1.276	0.003	0.009	0.050
64	236.07	−3.906	0.224	1.887	1.195	0.005	0.013	0.050
62	241.57	−3.784	0.213	1.721	1.093	0.008	0.018	0.050
60	247.07	−3.665	0.202	1.585	0.997	0.011	0.023	0.050
58	252.57	−3.548	0.191	1.482	0.922	0.015	0.029	0.050
56	258.08	−3.434	0.184	1.412	0.872	0.019	0.036	0.050
54	263.57	−3.322	0.181	1.364	0.846	0.022	0.044	0.050
52	268.71	−3.212	0.176	1.314	0.835	0.029	0.053	0.066
50	270.64	−3.104	0.169	1.248	0.832	0.036	0.067	0.094
48	270.36	−2.996	0.156	1.157	0.830	0.040	0.087	0.126
46	266.79	−2.887	0.141	1.055	0.832	0.043	0.114	0.163
44	261.37	−2.777	0.124	0.952	0.841	0.044	0.147	0.208
42	255.87	−2.663	0.109	0.862	0.859	0.043	0.179	0.254
40	250.38	−2.548	0.096	0.784	0.886	0.041	0.202	0.299
38	244.87	−2.429	0.085	0.715	0.918	0.035	0.205	0.325
36	239.37	−2.308	0.075	0.649	0.951	0.028	0.191	0.321
34	233.89	−2.184	0.065	0.587	0.977	0.019	0.165	0.290
32	229.07	−2.057	0.058	0.532	0.994	0.012	0.136	0.264
30	226.56	−1.928	0.052	0.485	0.998	0.007	0.111	0.254
28	224.55	−1.798	0.047	0.447	0.992	0.003	0.092	0.245
26	222.55	−1.666	0.042	0.414	0.983	0.000	0.073	0.225
24	220.55	−1.533	0.036	0.385	0.981	−0.003	0.057	0.207
22	218.56	−1.399	0.031	0.363	0.995	−0.005	0.041	0.160
20	216.95	−1.263	0.026	0.347	1.031	−0.006	0.029	0.122
18	216.66	−1.127	0.021	0.336	1.092	−0.007	0.020	0.050
16	216.65	−0.991	0.016	0.326	1.180	−0.005	0.014	0.050
14	216.65	−0.855	0.012	0.313	1.291	−0.002	0.007	0.050
12	216.65	−0.718	0.009	0.305	1.430	0.000	0.000	0.050
10	223.15	−0.583	0.007	0.310	1.588	0.000	0.000	0.050

dependent on the vertical scale and is contributed from the cool-to-space term. Negative values of $N_0^{O_3}(z)$ represent a radiative heating from the warm regions of stratopause and troposphere. The second term, which depends on the vertical wavenumber, is from the radiative heat exchange among the nearby layers. For the limit cases of $n \to 0$ and $n \to \infty$ we have

$$\lambda_r(z, 0) = N_0(z), \quad \lambda_r(z, \infty) = N_0(z) + N_\infty(z). \tag{19}$$

Based on (18) and (19), Fig. 6 shows that CO_2 makes a major contribution to the damping rate. The reason is that not only is the cooling rate by CO_2 for a reference temperature profile, which contributes mostly to $N_0(z)$, greater than by O_3, but also the atmosphere is more opaque to the CO_2 than to O_3 so the radiative heat exchange within the atmosphere for a perturbed temperature profile is more effective for CO_2. For example, we can see from Table 1 that $N_0^{CO_2}(z)$ at 48 km is four times greater than $N_0^{O_3}(z)$, whereas $N_\infty^{CO_2}(z)$ is 13 times greater than $N_\infty^{O_3}(z)$ at the same altitude. The H_2O concentration in the middle atmosphere is so low that the atmosphere is more transparent to H_2O than to CO_2. Furthermore, the cooling rate by H_2O around stratopause ($\sim$1 K day^{-1}) is only half of the cooling rate by O_3 (Chou et al. 1992). Therefore, the damping rate by H_2O is negligible. In Fig. 7 we compare the damping rates calculated from (18) with the exact values from Fig. 4 at four different altitudes. The figure shows that the fit is generally good over the whole range of vertical wavenumber with typical percentage errors of 10%–20%.

To incorporate a temperature variation we follow Fels (1982) and utilize a WKB approximation to obtain the parameterization of scale-dependent Newtonian damping rate for any temperature profile

$$\lambda(z, n; T) = \frac{(\partial\theta_2/\partial T)}{[\partial\theta_2/\partial T]_{T=T_r}} \lambda_r^{CO_2}(z, n) + \frac{(\partial\theta_3/\partial T)}{[\partial\theta_3/\partial T]_{T=T_r}} \lambda_r^{O_3}(z, n), \tag{20}$$

where $\lambda_r^{CO_2}(z, n)$ and $\lambda_r^{O_3}(z, n)$ are the damping rates of CO_2 and O_3 for a reference temperature profile T_r and are defined by (18) with the parameters given in Fig. 6. The coefficients due to the temperature variation, $\partial\theta_2/\partial T$ and $\partial\theta_3/\partial T$, are given by (6).

Remembering the definition (5) for the matrix **A** we recognize that the parameterization (20) only incorporates local temperature variations of the source functions θ_2 and θ_3. The nonlocal temperature variation of the Curtis matrices has been neglected. In appendix A it is shown for the cool-to-space approximation that the effect of temperature variation on cooling rate and damping rate is small. However, in the upper mesosphere the radiative heat exchange from the stratopause becomes significant. When calculated by a constant Curtis matrix, CO_2 cooling rate shows notable errors around the upper polar mesospheres where temperatures largely depart from the reference temperature (Zhu et al. 1992). The errors in cooling rate will be more effectively carried into damping rate of a temperature disturbance with a greater vertical scale. In the next section we will test our damping rate param-

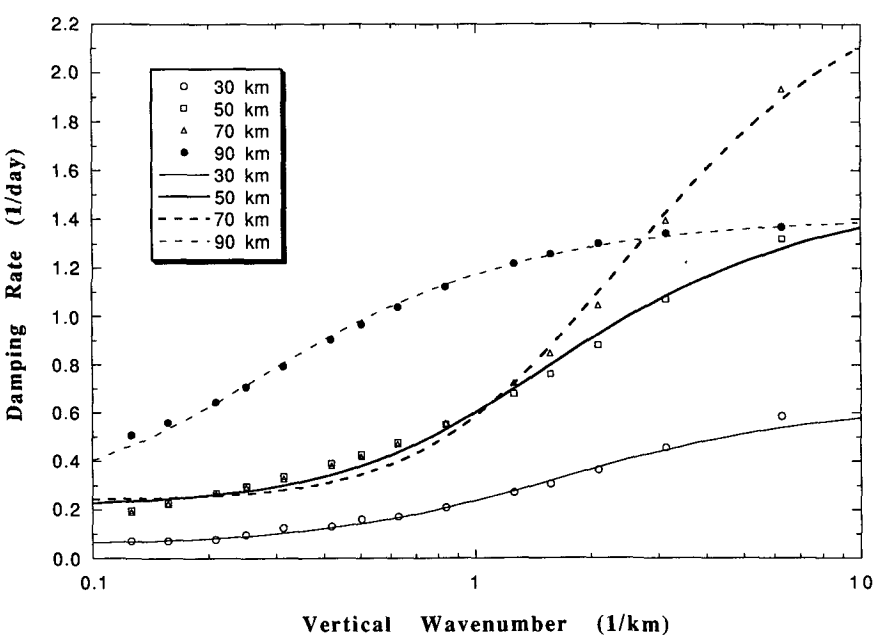

FIG. 7. Fitting the damping rates with the analytic expression (18) at 30, 50, 70, and 90 km, respectively.

eterization (18) and (20) by comparing its result with the exact damping rate calculated by the Curtis matrices that vary with temperature profiles.

4. Test of the damping rate parameterization

In this section we will calculate the global damping rate for the July temperature field of the CIRA 1986 reference atmosphere and an observed ozone mixing ratio distribution in July (Zhu et al. 1991). At each latitude the damping rate is calculated with the temperature and ozone profiles from surface to 120 km with a vertical resolution of 1 km. The Curtis matrices for CO_2 are calculated by the interpolation from the reference temperature profiles (Zhu 1990; Zhu et al. 1992). Similar interpolation schemes are also available for the O_3 mixing ratio variation. It is found that the difference is less than 20% if we calculate the O_3 cooling rate by a fixed Curtis matrix referenced to a global averaged O_3 mixing ratio. Since the damping rate contributed by O_3 cooling makes only a minor contribution to the total damping rate, we expect the errors to be small due to a fixed Curtis matrix $\mathbf{C}_3$ in (4).

Figure 8 presents the global cooling rate by CO_2 and O_3 for the July temperature field of the CIRA 1986 reference atmosphere. Because of the near-LTE nature of CO_2 15-μm band emission, the globally averaged cooling rate around 100 km reaches $\sim$15 K day^{-1}, which is significantly greater than the previous calculation (Zhu et al. 1992). It is found that globally averaged solar heating by O_2 and O_3 is about 10 K day^{-1}. The net radiative cooling rate of 5 K day^{-1} is balanced by a globally averaged downward heat flux due to molecular and eddy diffusion. The other notable feature in Fig. 8 is a huge contrast in cooling rate between summer and winter mesopause regions (80 km–90 km). This common feature exists in all CO_2 cooling rate calculations for solstice seasons. Because such a contrast is mostly carried into $N_0(z)$ in the damping rate calculation, we expect that the contrast in damping rate decreases as the vertical wavenumber increases.

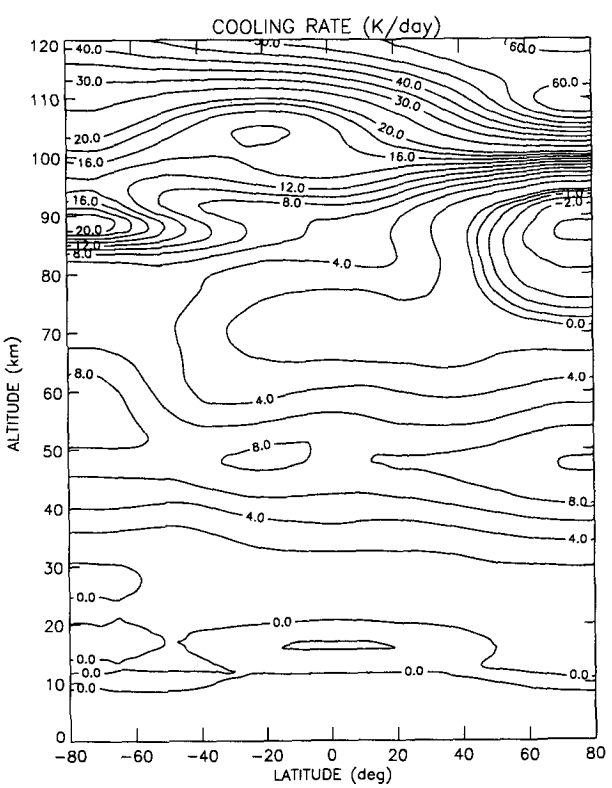

FIG. 8. Global cooling rate by CO_2 and O_3 for the July temperature field of the CIRA 1986 reference atmosphere and an observed ozone distribution.

In Fig. 9 we present the Newtonian damping rates for three different vertical wavelengths of 2, 5, and 15 km. In addition to the two pronounced characteristics shown in Fig. 4—scale dependence and a local maximum damping rate around the mesopause for small vertical wavelengths—Fig. 9 also shows that the damping rate in the winter polar mesosphere is greater than that in the summer polar mesosphere. The difference is more than a factor of 3 around the mesopause for a vertical wavelength of 5 km because the cooling rate in the winter polar mesopause is much greater than in the summer, as shown in Fig. 8. Even though the temperature disturbances are more strongly damped by radiation in the winter mesosphere than in the summer mesosphere, observed temperature perturbations still have larger amplitudes in the winter mesosphere than in the summer mesosphere (Theon and Smith 1970). This fact suggests that wave breaking plays a more important role than radiative damping for the gravity waves in the mesosphere. As pointed out in Zhu (1987), the lapse rate of the basic temperature field is greater in the summer mesosphere ($-d\bar{T}/dz$ = 3.2 K km^{-1}) than in the winter mesosphere ($-d\bar{T}/dz$ = 0.8 K km^{-1}). Therefore, a smaller temperature perturbation is adequate to satisfy the saturation criterion of $|d(\bar{T} + T')/dz|$ = 9.8 K km^{-1} (Lindzen 1981) for the wave breaking in the summer mesosphere than in the winter mesosphere.

Figure 10 shows the percentage errors resulting from the use of our simple parameterization formula to calculate the damping rate, $100 \times (\lambda_{ap} - \lambda_{ex})/\lambda_{ex}$, where λ_{ex} is from Fig. 9 and λ_{ap} is calculated from (18) and (20). The typical errors range from 10% to 20%. These errors consist in two parts. One comes from Fig. 7; that is, we have used an analytic formula (17) to express the kernel function in (14). The other part is the neglect of the temperature variation of the Curtis matrices, as discussed in the previous section.

5. Conclusions

We have calculated the radiative damping rates of the atmospheric temperature perturbations by both CO_2 15-μm band and O_3 9.6-μm band emissions from

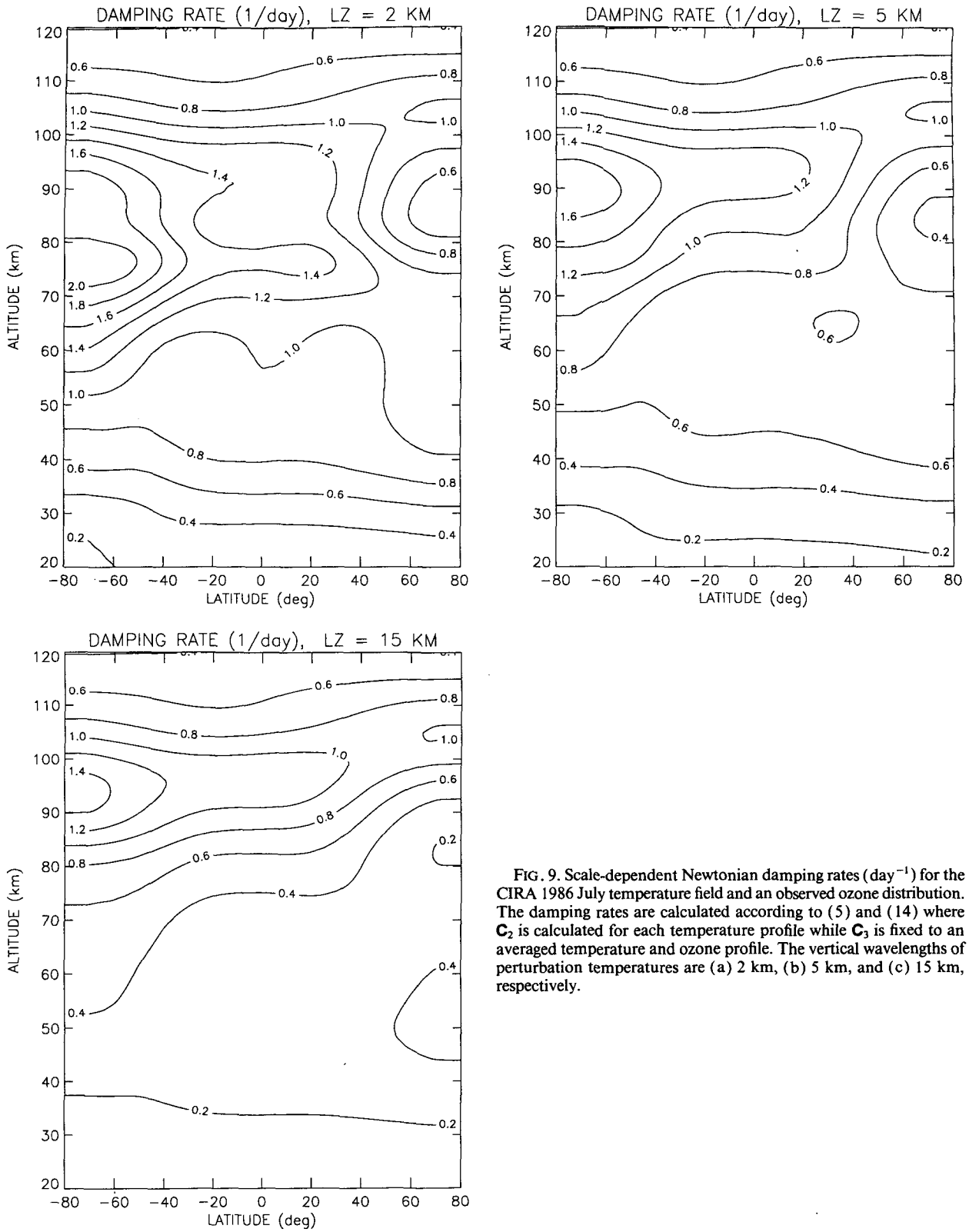

FIG. 9. Scale-dependent Newtonian damping rates (day^{-1}) for the CIRA 1986 July temperature field and an observed ozone distribution. The damping rates are calculated according to (5) and (14) where $\mathbf{C}_2$ is calculated for each temperature profile while $\mathbf{C}_3$ is fixed to an averaged temperature and ozone profile. The vertical wavelengths of perturbation temperatures are (a) 2 km, (b) 5 km, and (c) 15 km, respectively.

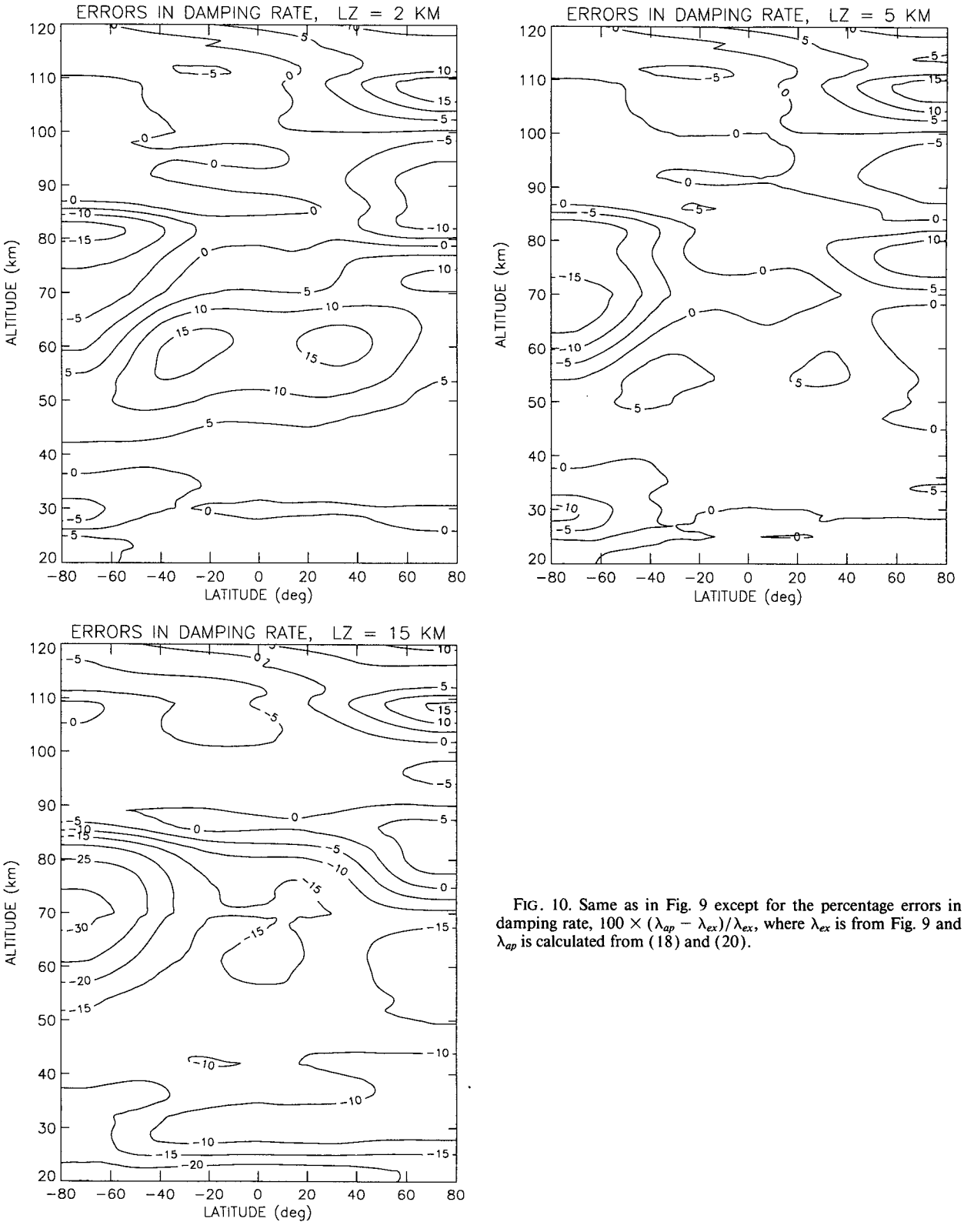

FIG. 10. Same as in Fig. 9 except for the percentage errors in damping rate, $100 \times (\lambda_{ap} - \lambda_{ex})/\lambda_{ex}$, where λ_{ex} is from Fig. 9 and λ_{ap} is calculated from (18) and (20).

the surface to 120 km. Based on a 242 × 242 Curtis matrix of a vertical resolution of 0.5 km both approaches of eigenvalue analysis and Newtonian cooling method are presented. The scale-dependent Newtonian damping rate provides a practically useful way to describe how a local wave packet with a characteristic vertical wavenumber is damped in an inhomogeneous atmosphere. A simple formula calculating the scale-dependent damping rate is also derived and is further tested for a zonally averaged model atmosphere for the month of July. Based on the latest value of the deactivation rate of CO_2 bending mode by atomic oxygen the radiative damping rate in the region of 90–100 km is $\sim 1.3\ \text{day}^{-1}$. This is four times greater than the one calculated by the previous deactivation rate and is comparable to the damping rate induced by eddy and molecular diffusion of $\sim 2.5\ \text{day}^{-1}$ in the corresponding region. It is also found that the radiative damping of the temperature perturbation in the winter polar mesopause is more than a factor of 3 greater than in the summer polar mesopause. The parameterization provides a relatively accurate damping rate with fractional errors of 10%–20%. The formulation can be used in any models of wave–zonal flow interactions in the earth's middle atmosphere.

Acknowledgments. The author wishes to thank Dr. Darrell F. Strobel for his perceptive comments on the original manuscript. Valuable comments by one reviewer on the interpretation of eigenvalue approach are also appreciated. The author also wishes to thank E. L. Fleming for his kindness in supplying the datasets of CIRA 1986 temperature fields. This research was supported by the MAP program of the Naval Research Laboratory and in part by NSF Grant ATM-9019376.

APPENDIX A

Temperature Variation Caused Changes in Damping Rate

Assuming nonoverlap Voigt line profiles and a radiation escape to space approximation, we can write the cooling rates in weak and strong limits in the following forms (Houghton 1986),

$$\text{weak limit:}\quad Q = \text{const} \times B(T) \times \left[\sum s_i\right] \tag{A1.a}$$

$$\text{strong limit:}\quad Q = \text{const} \times B(T) \times \left[\sum (s_i\alpha_i)^{1/2}\right] \tag{A1.b}$$

where $B(T)$ is the Planck blackbody function at the band center, s_i is the line strength, and α_i is the Lorentz half-width. For a given temperature variation the induced cooling rate variation or the Newtonian damping rate can be derived as

$$\text{weak limit:}\quad \lambda \equiv -\frac{dQ}{dT} = \text{const}\left\{S\frac{dB}{dT} + B\frac{dS}{dT}\right\} \tag{A2.a}$$

$$\text{strong limit:}\quad \lambda \equiv -\frac{dQ}{dT} = \text{const}\left\{R\frac{dB}{dT} + B\frac{dR}{dT}\right\} \tag{A2.b}$$

where $S = \sum s_i$ is the band strength and $R = \sum (s_i\alpha_i)^{1/2}$. In deriving (4) in section 2 we kept only the terms that were equivalent to the first term in (A2). To estimate the ratios of the second terms to the first in (A2) for CO_2 we note that from the band parameters S and R (Zhu 1991)

$$\frac{(\delta S/\delta T)}{S} \approx 2.8 \times 10^{-4}\ \text{K}^{-1},$$

$$\frac{(\delta R/\delta T)}{R} \approx 3.1 \times 10^{-3}\ \text{K}^{-1},\ \text{at}\ T = 260\ \text{K}. \tag{A3}$$

On the other hand, from (3a) and (6a) we have

$$\frac{(\delta B/\delta T)}{B} \approx 1.47 \times 10^{-2}\ \text{K}^{-1},\quad \text{at}\quad T = 260\ \text{K}. \tag{A4}$$

Therefore, the second terms in (A2.a,b) make ~2% and ~20% contributions to the total cooling in the weak and strong limits, respectively. Generally speaking, if the absorption is in weak (strong) limit the contribution to the radiation field mainly comes from the core (wings). Fels (1984, his Fig. 4) showed that the major contribution to the damping rate in the mesosphere is due to the line cores. We expect half of the core contribution in the stratosphere. Therefore, second terms in (A2.a,b) are about one order of magnitude smaller than the corresponding first terms. The damping rates in weak and strong limits can be approximated by

$$\text{weak limit:}\quad \lambda = \text{const} \times S \times \frac{dB}{dT} \tag{A5.a}$$

$$\text{strong limit:}\quad \lambda = \text{const} \times R \times \frac{dB}{dT}. \tag{A5.b}$$

Next, we examine the errors induced by using the Curtis matrix of a reference temperature profile to calculate the damping rate for any temperature profile as in the parameterization formula (15). From (A5) we get

$$\text{weak limit:}\quad \frac{\delta\lambda}{\lambda} = \frac{\delta(dB/dT)}{(dB/dT)} + \frac{\delta S}{S} \tag{A6.a}$$

$$\text{strong limit:}\quad \frac{\delta\lambda}{\lambda} = \frac{\delta(dB/dT)}{(dB/dT)} + \frac{\delta R}{R}. \tag{A6.b}$$

Similar to (A2) we can show again that the major contribution to $\delta\lambda/\lambda$ in (A6) comes from the first terms.

REFERENCES

Apruzese, J. P., and D. F. Strobel, 1984: Radiative relaxation rates for individual 15-μm CO_2 lines in the upper stratosphere and lower mesosphere. *J. Geophys. Res.*, **89**, 7187–7194.

Chou, M. D., D. P. Kratz, and W. Ridgway, 1991: Infrared radiation parameterizations in numerical climate models. *J. Climate,* **4,** 424–437.

Dickinson, R. E., 1973: Method of parameterization for infrared cooling between altitudes of 30 and 70 kilometers. *J. Geophys. Res.,* **78,** 4451–4457.

——, 1984: Infrared radiative cooling in the mesosphere and lower thermosphere. *J. Atmos. Terr. Phys.,* **46,** 995–1008.

Fels, S. B., 1982: A parameterization of scale-dependent radiative damping rates in the middle atmosphere. *J. Atmos. Sci.,* **39,** 1141–1152.

——, 1984: The radiative damping of short vertical scale waves in the mesosphere. *J. Atmos. Sci.,* **41,** 1755–1764.

——, and M. D. Schwarzkopf, 1981: An efficient, accurate algorithm for calculating CO_2 15 μm band cooling rates. *J. Geophys. Res.,* **86,** 1205–1232.

Goody, R. M., and Y. L. Yung, 1989: *Atmospheric Radiation: Theoretical Basis.* second ed. Oxford University Press, 519 pp.

Holton, J. R., 1983: The influence of gravity wave breaking on the general circulation of the middle atmosphere. *J. Atmos. Sci.,* **40,** 2497–2507.

Houghton, J. T., 1986: *The Physics of Atmospheres.* second ed. Cambridge University Press, 271 pp.

Kutepov, A. A., and G. M. Shved, 1978: Radiative transfer in the 15-μm CO_2 band with the breakdown of local thermodynamic equilibrium in the earth's atmosphere. *Izv., Atmos. Oceanic Physics,* **14,** 18–30.

Lancaster, P., 1969: *Theory of Matrices.* Academic Press, 316 pp.

Lindzen, R. S., 1981: Turbulence and stress due to gravity wave and tidal breakdown. *J. Geophys. Res.,* **86,** 9707–9714.

Lopez-Puertas, M., R. Rodrigo, A. Molina, and F. W. Taylor, 1986: A non-LTE radiative transfer model for infrared bands in the middle atmosphere. I. Theoretical basis and application to CO_2 15 μm bands. *J. Atmos. Terres. Phys.,* **48,** 729–748.

——, M. A. Lopez-Valverde, and F. W. Taylor, 1992: Vibrational temperature and radiative cooling of the CO_2 15 μm bands in the middle atmosphere. *Quart. J. Roy. Meteor. Soc.,* **118,** 499–532.

Press, W. H., B. P. Flannery, S. A. Teukolsky, and W. T. Vetterling, 1986: *Numerical Recipes. The Arts of Scientific Computing.* Cambridge University Press, 702 pp.

Schwarzkopf, M. D., and S. B. Fels, 1985: Improvements to the algorithm for computing CO_2 transmissivities and cooling rates. *J. Geophys. Res.,* **90,** 10 541–10 550.

Sharma, R. D., and P. P. Wintersteiner, 1990: Role of carbon dioxide in cooling planetary atmospheres. *Geophys. Res. Lett.,* **17,** 2201–2204.

Shved, G. M., 1978: Influence of radiative transfer on certain types of motions in planetary atmospheres. *Adv. Heat Transfer,* **14,** 249–280.

——, and D. P. Utyakovskiy, 1983: Radiative damping of temperature perturbations in the earth's upper atmosphere, taking into account the breakdown of local thermodynamic equilibrium. *Izv., Atmos. Oceanic Phys.,* **19,** 353–357.

——, L. E. Khvorostovskaya, I. Yu. Potekhin, A. I. Dem'Yanikov, A. A. Kutepov, and V. I. Fomichev, 1991: Measurement of the quenching rate constant of $CO_2(0100)$-O collisions and its significance for the thermal regime and radiation in the lower thermosphere. *Izvestiya, Atmos. Oceanic Physics,* **27,** 295–299.

Spiegel, E. A., 1957: The smoothing of temperature fluctuations by radiative transfer. *Astrophys. J.,* **126,** 202–207.

Strobel, D. F., 1989: Constraints on gravity wave induced diffusion in the middle atmosphere. *Pure and Appl. Geophys.,* **130,** 533–546.

Theon, J. S., and W. S. Smith, 1970: Seasonal transitions in the thermal structure of the mesosphere at high latitudes. *J. Atmos. Sci.,* **27,** 173–176.

U.S. Standard Atmosphere, 1976, NOAA-S/T76-1562, Supt. of Documents, U.S. Govt. Printing Office, Washington, D.C.

Wintersteiner, P. P., R. H. Picard, R. D. Sharma, J. R. Winick, and R. A. Joseph, 1992: Line-by-line radiative excitation model for the non-equilibrium atmosphere: Application to CO_2 15 μm emission. *J. Geophys. Res.,* **97,** 18 083–18 117.

Zhu, X., 1987: Inertio–gravity waves in the middle atmosphere. Ph.D. thesis, University of Washington, Seattle, Washington, 165 pp.

——, 1990: Carbon dioxide 15-μm band cooling rates in the upper middle atmosphere calculated by Curtis matrix interpolation. *J. Atmos. Sci.,* **47,** 755–774.

——, 1991: Spectral parameters in band models with distributed line intensity. *J. Quant. Spectrosc. Radiat. Transfer,* **45,** 33–46.

——, 1992: The correlated-k coefficients calculated by random band models. *J. Quant. Spectrosc. Radiat. Transfer,* **47,** 159–170.

——, and D. F. Strobel, 1991: Radiative damping in the upper mesosphere. *J. Atmos. Sci.,* **48,** 184–199.

——, M. E. Summers, and D. F. Strobel, 1991: Analytic models for the ozone radiative absorption rate at 9.6 μm in the mesosphere. *J. Geophys. Res.,* **96,** 18 551–18 559.

——, ——, and ——, 1992: Calculation of CO_2 15 μm band atmospheric cooling rates by Curtis matrix interpolation of correlated-k coefficients. *J. Geophys. Res.,* **97,** 12 787–12 797.